Contraction of surfactant-laden pores

Jiakai Lu,[†] Diego M. Campana,[‡] and Carlos M. Corvalan[*,†]

†*Transport Phenomena Laboratory, Department of Food Science, Purdue University, West Lafayette, IN 47907, USA*

‡*Centro de Investigaciones y Transferencia de Entre Ríos, CONICET-UNER. Facultad de Ingeniería, Universidad Nacional de Entre Ríos, Ruta 11 (Km. 10), 3100 (Oro Verde), Entre Ríos, República Argentina*

E-mail: corvalac@purdue.edu

Abstract

The contraction of surfactant-laden pores at the microscale has implications for natural and technological processes ranging from the collapse of channels in lipid membranes to the stability of foams in the food processing industry. Despite its prevalence, our understanding of the mechanisms of pore contraction in the presence of surfactants remains unclear. These mechanisms have been challenging to study experimentally given the small length scale near the singularity and simulations capable of accurately characterizing the pore dynamics may help enhance our understanding of the process. Here, we use high-fidelity numerical simulations to gain insight into the fluid dynamics and interfacial phenomena underlying the contraction of viscous pores in the presence of an insoluble surfactant. The simulations show that surfactants accumulate on the advancing front of a collapsing pore due to the uneven deformation of the pore interface. Because of this accumulation, even a small amount of surfactant plays a major role in the way in which a collapsing pore approaches the singularity.

keywords: pore, nanopore, surfactant, free-surface, DNA sequencing

Introduction

The contraction of surfactant-laden pores at the micron and submicron scale is a critical phenomenon in nature, as in the collapse of pores in lipid membranes[1,2], and central to technological systems ranging from the processing of foams in the food industry to the fabrication of nanopore-based sensors for analysis of nucleic acids and proteins[3–6]. Currently, there is a good understanding of the fluid dynamics of both expanding[7–9] and contracting pores[10–12] for fluids with clean interface. But a recent theoretical and experimental study by Petit et al.[13] has highlighted the major role that the presence of surface-active species may play modulating the pore dynamics. Petit et al.[13] observed that opening pores nucleated in a soap film with strong surface elasticity expand at a velocity that is significantly smaller than the Taylor-Culick velocity expected from the balance between inertia and the equilibrium surface tension of the film[7,8]. This deviation from the theoretical Taylor-Culick velocity was attributed to local gradients of surface tension resulting from the transport of the surface-active species on the soap film.

The findings by Petit et al.[13], as well as other previous works[14,15], provide important insights into the influence of surfactants on the dynamics of opening pores. But the role of surfactants on the fluid dynamics of contracting pores is still largely unknown, in part due to the small length scale of the process near the singularity. In particular, how surface-active species disperse through the deforming pore interface during the contraction of small pores, and how the resulting changes in the local surface tension affect the velocity of contraction, remains an open question. Here, we address this question for the case of viscous pores covered with an small amount of an insoluble surfactant. We characterize the fluid dynamics and interfacial phenomena underlying the contraction of the pores using high-fidelity simulations that simultaneously solve the full Navier-Stokes system that governs the free-surface flow and the convection-diffusion equation that governs the surfactant transport. Results reveal that, contrary to viscous pores with clean interface, which contract at constant speed[12], surfactant-laden pores contract at progressively decreasing speed. This new behavior, the

simulations show, results from the continuous accumulation of the surface-active species on the advancing front of the pore. Because of this accumulation, even a tiny amount of the surfactant may play a major role in the way in which a collapsing pore approaches the singularity.

Free-surface Model and Methods

A sufficiently small pore nucleated in a liquid sheet will contract, and eventually collapse, driven by capillary forces associated with its small radius of curvature[7]. Here, we consider the capillary contraction of a small circular pore nucleated in a viscous fluid sheet of thickness H. The fluid is a Newtonian liquid of constant density ρ and large viscosity μ, uniformly covered with an insoluble surfactant of concentration γ_0 (Fig. 1).

Recently, Savva and Bush[9] investigated the dynamics of opening pores using a one-dimensional lubrication approximation that exploits the small thickness of the liquid sheet. This approximation has been shown to accurately predict pore expansion[11,12] but it cannot predict the evolution of closing pores because the thickness-to-radius ratio grows unbounded as the pore collapses. Therefore, to study the free-surface dynamics of collapsing pores, we have developed high-fidelity simulations that overcome the limitations of the lubrication model by solving the full Navier-Stokes governing equations. The model is described below in dimensionless form using H as lengthscale, γ_0 as concentration scale, and $V \equiv \sigma_0/\mu$, where σ_0 is the equilibrium surface tension corresponding to the surfactant concentration γ_0, as velocity scale. The contraction of the pore is analyzed by solving the full axisymmetric Navier-Stokes equations

$$\mathrm{Re}(\partial \mathbf{v}/\partial t + \mathbf{v} \cdot \nabla \mathbf{v}) = \nabla \cdot \mathbf{T}, \tag{1}$$

$$\nabla \cdot \mathbf{v} = 0, \tag{2}$$

where $\mathrm{Re} \equiv \rho V H/\mu$ is the Reynolds number and where the influence of gravity is considered

negligible. The stress tensor $\mathbf{T} = -p\mathbf{I} + [(\nabla\mathbf{v}) + (\nabla\mathbf{v})^T]$, where p is pressure and $\mathbf{v}$ the fluid velocity. The fluids does not cross the free interface, which is ensured by imposing the kinematic boundary condition along the pore surface

$$\mathbf{n} \cdot (\mathbf{v} - \mathbf{v}_s) = 0, \tag{3}$$

where $\mathbf{n}$ is the unit normal vector to the free surface and $\mathbf{v}_s$ is the velocity of the points on the interface.

The driving surface tension σ is coupled to the fluid flow through the traction condition along the pore interface

$$\mathbf{T} \cdot \mathbf{n} = \sigma(2\mathcal{H})\mathbf{n} + \nabla_s\sigma, \tag{4}$$

where $\mathcal{H}$ in the capillary stress term is the mean surface curvature, and $\nabla_s \equiv (\mathbf{I} - \mathbf{nn}) \cdot \nabla$ in the Marangoni stress term is the surface gradient operator[16]. The time evolution of the surfactant concentration γ along the pore interface is tracked by the transport equation

$$\partial\gamma/\partial t + \gamma(\mathbf{v}_s \cdot \mathbf{n})(\nabla_s \cdot \mathbf{n}) + \nabla_s \cdot (\gamma\mathbf{v}_s \cdot \mathbf{t})\mathbf{t} - Pe^{-1}\nabla_s^2\gamma = 0, \tag{5}$$

which accounts for surfactant transport due to convection (third term), diffusion (fourth term), and surface dilatation (second term)[17,18]. For realistic values of the surfactant diffusion coefficient D, the Peclet number $Pe \equiv HV/D \gg 1$. We use $Pe = 10^3$ in our simulations unless stated; the results indicate that this value is sufficiently large that further increases do not significantly affect the pore dynamics for the ranges of parameters studied in this work. Following Hansen et al.[19], Campana and Saita[20] and Dravid et al.[21], we assume that the surface tension and surfactant concentration fields are related using a linear surface equation of state

$$\sigma = 1 - Ma(\gamma - 1) \tag{6}$$

so that surface activity is represented by a single parameter, the Marangoni number Ma.

The pore is considered axisymmetric around the z-axis, and symmetry boundary conditions are applied on the plane of symmetry $z = 0$.

Following Lu and Corvalan[11], the set of governing equations was discretized in space using the finite-element method, along with an arbitrary Lagrangian-Eulerian scheme in which the location of the free interface is traced using the method of spines introduced by Kistler and Scriven[22]. The time derivatives were discretized using the finite-difference method, with an Adam-Bashforth predictor and trapezoidal rule corrector in which the time steps were adaptively calculated using first-order continuation[23]. Finally, the non-linear system was solved simultaneously for velocity, pressure, surfactant concentration and location of the free interface using a full Newton's method in which the entries of the Jacobian were calculated analytically as described in Kistler and Scriven[22] to enhance convergence. We have repeatedly verified this algorithm by contrasting its predictions against available analytical solutions and experimental data during the analysis of both viscous and inertial nanopores[11,12], as well as surfactant-laden drops[18], fibers[24] and filaments[21].

Results and Discussion

The contraction of tiny pores nucleated in viscous fluid films has been examined in experiments by Storm et al.[25],[26] and Wu et al.[6] motivated by the development of nanopore-based sensors for sequencing nucleic acids and analyzing epigenetic modifications[3]. These experiments have revealed that in the absence of surfactants viscous nanopores contract at constant speed when approaching collapse.

As recently confirmed by computations in Lu et al.[12], this constant terminal speed results from an eventual equilibrium between viscous and capillary forces, and thus corresponds to $U = \sigma_0/(2\mu)$ for pores with large viscosity μ and constant surface tension σ_0. Extending the work in Lu et al.[12], here we present results from high-fidelity simulations of pore contraction that take into account the effect of surfactants. Particular attention is given to the influence

of contaminants on the speed of contraction.

Influence of surfactants on the speed of contraction

To gain preliminary insight into how the presence of contaminants affects the pore dynamics, we show in Figure 2 the computed pore velocity v_m as a function of minimum pore radius r_m for two viscous pores with Marangoni numbers $Ma = 5 \times 10^{-4}$ (red line) and 1×10^{-3} (blue line). The pores are nucleated in a liquid sheet with small Reynolds number $Re = 0.5$. As a benchmark, and to compare our results to those expected for pores with constant surface tension, the figure also includes the computed pore speed for an otherwise identical pore with $Ma = 0$ (black line). The figure follows the contraction of the pores for about three decades, from the initial dimensionless radius $r_m = 0.1$ to a final radius $r_m \approx 3 \times 10^{-4}$, or approximately 30 nm for a 100 μm thick fluid sheet.

Despite the small Marangoni numbers, the results show a significant qualitative difference between the pores with $Ma = 0$ and those with $Ma \neq 0$. For the pore with $Ma = 0$, the interfacial tension remains constant on the surface of the pore until collapse (Eq. 6). Accordingly, the pore eventually attains a constant terminal speed, as observed in experiments for pores with constant surface tension during the late stage of contraction[6,25]. Furthermore, the terminal speed corresponds to the theoretical viscous-capillary velocity $U = \sigma_0/(2\mu)$, which translates to $u = 1/2$ in the dimensionless scale of Figure 2 (dashed line). For the pores with $Ma \neq 0$, the interfacial tension changes dynamically on the surface of the pores due to surfactant diffusion, surfactant convection or area dilatation (Eqs. 5 and 6). As a result, the pores do not attain a constant terminal speed; rather, they contract at continuously decreasing speed after the initial transient. By the time the pore with $Ma = 1 \times 10^{-3}$ reaches $r_m = 3 \times 10^{-4}$, the speed of contraction is about 20% slower than the viscous-capillary velocity u based on the equilibrium surface tension.

The interfacial stress balance helps understand the qualitative difference between the two dynamics and leads, in the next section, to a simple scaling of the decreasing pore

speed with pore size. Indeed, as discussed in Figure 2, viscous pores with clean interface contract with constant speed $\sigma_0/(2\mu)$ due to the eventual equilibrium between viscous and capillary stresses. But this equilibrium is affected by the presence of surfactants in two ways. First, surfactants modify the capillary stress by lowering the dynamic surface tension and, second, they introduce Marangoni stresses into the stress balance (Eq. 4). However, at low Marangoni numbers, Marangoni stresses are not sufficient to displace the equilibrium (see below), and thus the viscous-capillary equilibrium still applies provided that the constant surface tension σ_0 is replaced by the dynamic surface tension. Therefore, for surfactants with low Marangoni numbers the velocity of contraction can be estimated as $\hat{\sigma}_m(t)/(2\mu)$, which in dimensionless form becomes

$$v_m(t) \approx \sigma_m(t)/2, \tag{7}$$

where $\sigma_m = \hat{\sigma}_m/\sigma_0$ is the instantaneous surface tension at the tip of the pore. As shown in Figure 3, the computed pore velocities agree reasonably well with this estimation for pores with low Marangoni numbers and a wide range of Peclet numbers $10 \leq Pe \leq 10^3$.

Evolution of the dynamic surface tension

Analyzing the mechanisms of surfactant transport, and the corresponding evolution of the surface tension $\sigma_m(t)$ is important to understanding the new pore dynamics. To illustrate these mechanisms, Figure 4 shows the spatial and temporal evolution of the interfacial tension for the pore of Figure 2 with $Ma = 1 \times 10^{-3}$. Results show a highly localized decrease of the surface tension within a narrow band on the advancing pore front (Fig. 4a). On this narrow band, the surface tension exhibits a minimum at the tip of the pore ($z = 0$), rises sharply as we move away from the tip, and finally levels out approaching the dimensionless initial value $\sigma = 1$ on the surface of the liquid sheet (Fig. 4b). Interestingly, the results also show that the interfacial tension at the pore front decreases as the pore contracts. The contraction speed is thus progressively slowed down due to the continuous weakening of the driving interfacial tension.

As may be expected, the local decrease of the surface tension is caused by accumulation of surfactant around the tip of the pore. The appropriate scaling for the surfactant accumulation is readily estimated. As a pore collapses, the surface area of the pore front contracts, and this contraction is most severe at the tip where the local surface area decreases proportional to the pore circumference. As a result, the surfactant concentration γ_m at the tip of the pore increases proportional to the inverse pore radius; that is, $\gamma_m \sim r_m^{-1}$. This scaling, along with the results in Figure 2, highlights an interesting characteristics of the pore dynamics — even a modest amount of surfactant is eventually capable of unexpectedly large effects due to surfactant crowding. Results in Figure 5 show that as the pore of Figure 2 with $Ma = 1 \times 10^{-3}$ contracts, the scaling $\gamma_m \sim r_m^{-1}$ (dashed line) agrees well with the simulations (black symbols). However, because the surfactant concentration must remain finite as $r_m \to 0$, the scaling is necessarily an intermediate one and must yield to a different dynamics as the pore moves even closer to the singularity. Moreover, because diffusion mitigates the accumulation process, the surfactant concentration γ_m should also depend on the Peclet number. Indeed, comparison of the simulations for Peclet numbers $Pe = 10$ (blue), 100 (red) and 1000 (black) reveals that there is a transition between the dilatation and the diffusion dominated regimes of surfactant transport. Results in Figure 5 show that as the Peclet number decreases, diffusion effects eventually becomes comparable to area-dilatation effects, and ultimately diffusion effects dominate the dynamics ($Pe \approx 10$).

The foregoing results suggest that for realistic values of the Peclet number (for which surfactant transport is dominated by area dilatation) the normalized pore velocity $s \equiv (u - v_m)/u$ can be estimated in function of the Marangoni number and instantaneous pore size as:

$$(s - Ma)/Ma \sim r_m^{-1}. \tag{8}$$

This results from using the surface equation of state to substitute σ_m in Equation 7, and then introducing the scaling of γ_m with the inverse pore radius. Taking into account that this relationship applies to contaminants with low Marangoni numbers, the scaling can be

further simplified to

$$s/Ma \sim r_m^{-1}. \tag{9}$$

This provides a simple scaling of the decreasing pore speed with pore size. As illustrated in Figure 6, the scaling (dashed line) agrees well with results from the full numerical simulations (symbols) at the later times of contraction.

Influence of interfacial stresses on the interfacial velocity field

A close examination of the flow field developed during the contraction of the pores reveals that surfactants may also play an important role on the interfacial velocity profiles. In this subsection, we briefly discuss the separate influence of the capillary and Marangoni stresses on the interfacial velocity field near collapse.

In the absence of surfactants the maximum interfacial velocity always occurs at the tip of the pore where the curvature is largest. The reason for this is that when the interfacial tension is constant the distribution of the capillary forces driving contraction is defined solely by the local curvature. In the presence of surfactants, however, the distribution of the capillary forces $(\mathbf{n} \cdot \mathbf{T} \cdot \mathbf{n}) = \sigma(\nabla \cdot \mathbf{n})$ at the interface is defined not only by the local curvature $\nabla \cdot \mathbf{n}$ but also by the distribution of the local surface tension $\sigma(\mathbf{x}; t)$. To illustrate the effect of the evolving surface tension, we compare in Figure 7 the interfacial velocity profiles for the pores of Figure 6 with $Ma = 1 \times 10^{-4}$, $Ma = 5 \times 10^{-4}$, and $Ma = 1 \times 10^{-3}$ at an intermediate time and at the imminence of collapse (minimum pore radii $r_m = 0.095$ and 3×10^{-4} respectively). Results show that because of the progressive decrease of the surface tension at the tip of the pore there is a qualitative change in the flow pattern when approaching collapse. The location of the maximum interfacial velocity switches from the tip of the pore at $z = 0$ (black lines) to two peaks about the midplane (blue lines).

The rapid contraction of the surface area not only lowers the local surface tension around the tip of the pore but also creates steep surface tension gradients, particularly at high Peclet numbers (see Fig. 4). In turn, surface tension gradients induce Marangoni stresses, which

act tangential to the interface (Eq. 4). These stresses cannot directly affect the interfacial shape but could modulate the velocity field near the interface through the tangential stress condition $(\mathbf{n}\cdot\mathbf{T}\cdot\mathbf{t}) = \mathbf{t}\cdot\nabla_s\sigma$. Figure 8, illustrates the influence of the Marangoni stresses on the interfacial tangential velocity for the pores with the lowest ($Ma = 1\times10^{-4}$) and highest ($Ma = 1\times10^{-3}$) Marangoni numbers in Figure 7. The Marangoni stresses are zero at the tip of the pore because of symmetry, then grow rapidly as we move away from the tip to reach a maximum value and finally decrease as we approach the surface of the liquid sheet where the surfactant concentrations remains essentially constant (Fig. 8a). Despite the different values of the Marangoni stresses, they have a negligible influence on the tangential interfacial velocity for the small Marangoni numbers used in this work (Fig. 8b).

Conclusion

In conclusion, results from our numerical study reveal that surfactant-laden pores collapse at progressively decreasing speed due to surfactant accumulation on the advancing front of the pore. As a consequence of this accumulation even a small amount of contaminant can drastically reduce the speed of contraction. These findings provide new mechanistic insights into the flow physics of surfactant-laden pores at low Marangoni numbers, and suggest interesting directions for future studies. For example, considering the strong influence that modest concentrations of surfactants have on the speed of contraction, it would be of interest to investigate the use of small pores as analytical tools for interfacial rheological characterization of dilute surfactants.

In addition, although our direct numerical simulations solve the full Navier-Stokes system that governs the free-surface flow along with the full convection-diffusion equation that governs the interfacial surfactant transport, the results are still limited by simplifying constitutive assumptions, including negligible surfactant solubility and linear surface equation of state. We expect that our results would motivate the further development of simulations

that incorporate soluble surfactants. Due to the surfactant accumulation at the pore front, it is conceivable that solubility may play an important role in the pore dynamics. Insoluble surfactants cannot easily leave the concentrated front region leading to a large drops of the interfacial tension; but surfactant solubility might mitigate this effect by enabling transfer of surfactant from the concentrated region to the bulk liquid[20]. Similarly, although contamination of the pore interface by a surfactant monolayer is a common situation, a more sophisticated surface equation of state would enable the study of high surfactant concentrations with micelles formation. In these conditions, the surface tension in the concetrated region may eventually take a constant equilibrium value as the pore contracts, potentially stabilizing the pore velocity.

Acknowledgement

This work was partially supported by the USDA National Institute of Food and Agriculture, Hatch projects 1008409 and 199888. D. C. would like to thank the following institutions for financial support: Consejo Nacional de Investigaciones Científicas y Técnicas of Argentina (CONICET) and Universidad Nacional de Entre Ríos (UNER).

References

(1) Chanturiya, A.; Chernomordik, L. V.; Zimmerberg, J. Flickering fusion pores comparable with initial exocytotic pores occur in protein-free phospholipid bilayers. *Proceedings of the National Academy of Sciences* **1997**, *94*, 14423–14428.

(2) Photos, P. J.; Bermudez, H.; Aranda-Espinoza, H.; Shillcock, J.; Discher, D. E. Nuclear pores and membrane holes: generic models for confined chains and entropic barriers in pore stabilization. *Soft Matter* **2007**, *3*, 364–371.

(3) Dekker, C. Solid-state nanopores. *Nature Nanotechnology* **2007**, *2*, 209–215.

(4) Iqbal, S. M.; Akin, D.; Bashir, R. Solid-state nanopore channels with DNA selectivity. *Nature nanotechnology* **2007**, *2*, 243–248.

(5) Iqbal, S. M.; Bashir, R. *Nanopores: sensing and fundamental biological interactions*; Springer Science & Business Media, 2011.

(6) Wu, S.; Park, S. R.; Ling, X. S. Lithography-free formation of nanopores in plastic membranes using laser heating. *Nano letters* **2006**, *6*, 2571–2576.

(7) Taylor, G. I. The Dynamics of Thin Sheets of Fluid. III. Disintegration of Fluid Sheets. *Proceedings of the Royal Society of London A* **1959**, *253*, 313–321.

(8) Culick, F. E. C. Comments on ruptured soap film. *Journal of Applied Physics* **1960**, *31*, 1128–1129.

(9) Savva, N.; Bush, J. W. M. Viscous sheet retraction. *Journal of Fluid Mechanics* **2009**, *626*, 211 – 240.

(10) Taylor, G. I.; Michael, D. H. On making holes in a sheet of fluid. *Journal of Fluid Mechanics* **1973**, *4*, 625.

(11) Lu, J.; Corvalan, C. M. Free-surface dynamics of small pores. *Chemical Engineering Science* **2015**, *132*, 93–98.

(12) Lu, J.; Yu, J.; Corvalan, C. M. Universal scaling law for the collapse of viscous nanopores. *Langmuir* **2015**, *31*, 8618–8622.

(13) Petit, P.; Le Merrer, M.; Biance, A.-L. Holes and cracks in rigid foam films. *Journal of Fluid Mechanics* **2015**, *774*, R3.

(14) McEntee, W. R.; Mysels, K. J. Bursting of soap films. I. An experimental study. *The Journal of Physical Chemistry* **1969**, *73*, 3018–3028.

(15) Frankel, S.; Mysels, K. J. Bursting of soap films. II. Theoretical considerations. *The Journal of Physical Chemistry* **1969**, *73*, 3028–3038.

(16) Slattery, J. C. *Interfacial Transport Phenomena*; Springer, New York, 1990.

(17) Wong, H.; Rumschitzki, D.; Maldarelli, C. On the surfactant mass balance at a deforming fluid interface. *Physics of Fluids (1994-present)* **1996**, *8*, 3203–3204.

(18) Lu, J.; Corvalan, C. M. Coalescence of viscous drops with surfactants. *Chemical Engineering Science* **2012**, *78*, 9–13.

(19) Hansen, S.; Peters, G.; Meijer, H. The effect of surfactant on the stability of a fluid filament embedded in a viscous fluid. *Journal of Fluid Mechanics* **1999**, *382*, 331–349.

(20) Campana, D.; Saita, F. Numerical analysis of the Rayleigh instability in capillary tubes: The influence of surfactant solubility. *Physics of Fluids* **2006**, *18*, 022104.

(21) Dravid, V.; Songsermpong, S.; Xue, Z.; Corvalan, C. M.; Sojka, P. E. Two-dimensional modeling of the effects of insoluble surfactant on the breakup of a liquid filament. *Chemical engineering science* **2006**, *61*, 3577–3585.

(22) Kistler, S. F.; Scriven, L. E. *Coating Flow: Computational Analysis of Polymer Processing*; Applied Science Publishers, New York, 1983.

(23) Corvalan, C. M.; Saita, F. A. Automatic stepsize control in continuation procedures. *Computers & Chemical Engineering* **1991**, *15*, 729–739.

(24) Campana, D. M.; Ubal, S.; Giavedoni, M. D.; Saita, F. A. Dip Coating of Fibers in the Visco-inertial Regime: Numerical Analysis. *Industrial & Engineering Chemistry Research* **2013**, *52*, 12646–12653.

(25) Storm, A. J.; Chen, J. H.; Ling, X. S.; Zandbergen, H. W.; Dekker, C. Electron-beam-induced deformations of SiO2 nanostructures. *Journal of Applied Physics* **2005**, *98*.

(26) Storm, A. J.; Chen, J. H.; Ling, X. S.; Zandbergen, H. W.; Dekker, C. Fabrication of solid-state nanopores with single-nanometre precision. *Nature Materials* **2003**, *2*, 537–540.

Figures

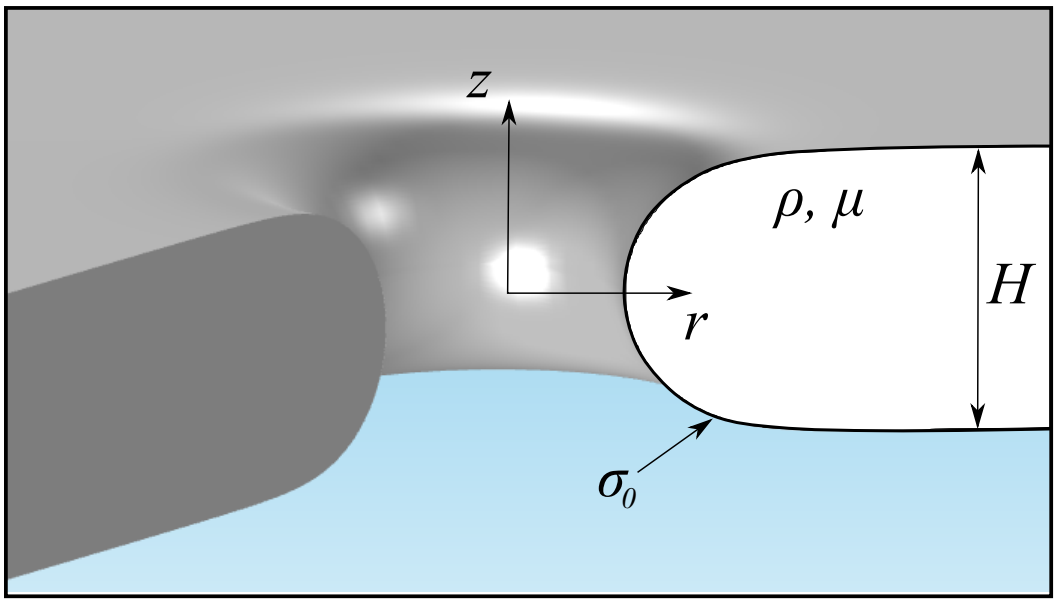

Figure 1: **Pore sketch.** Small circular pore nucleated in a Newtonian liquid sheet with density ρ, viscosity μ, and thickness H. The initial surface tension σ_0 is uniform, and corresponds to the initial surfactant concentration γ_0.

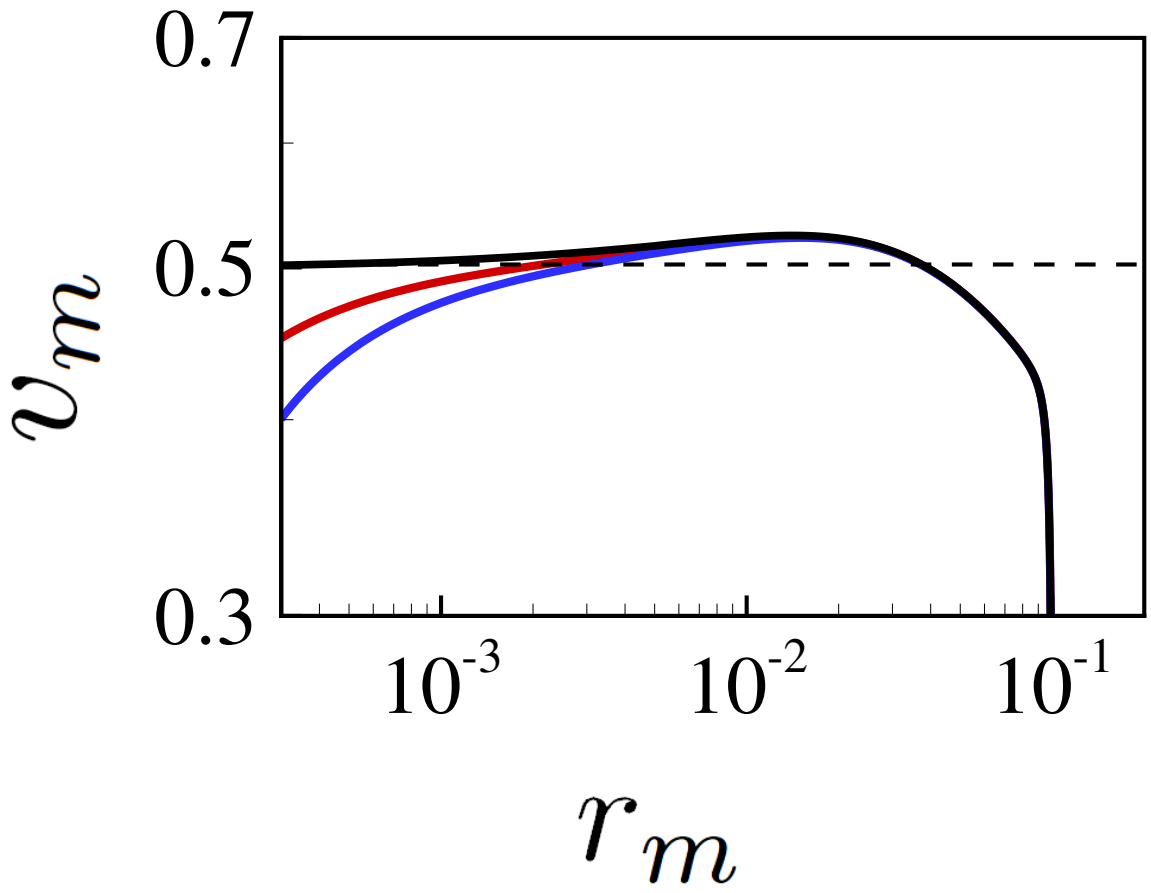

Figure 2: **Effect of surfactant on the contraction of a small viscous pore.** Evolution of the velocity of contraction v_m with the minimum pore radius r_m for pores with $Ma = 0$ (black line), $Ma = 5 \times 10^{-4}$ (red line), and $Ma = 1 \times 10^{-3}$ (blue line). The pore with $Ma = 0$ eventually approaches the theoretical viscous-capillary velocity $U = \sigma_0/(2\mu)$ (dashed line).

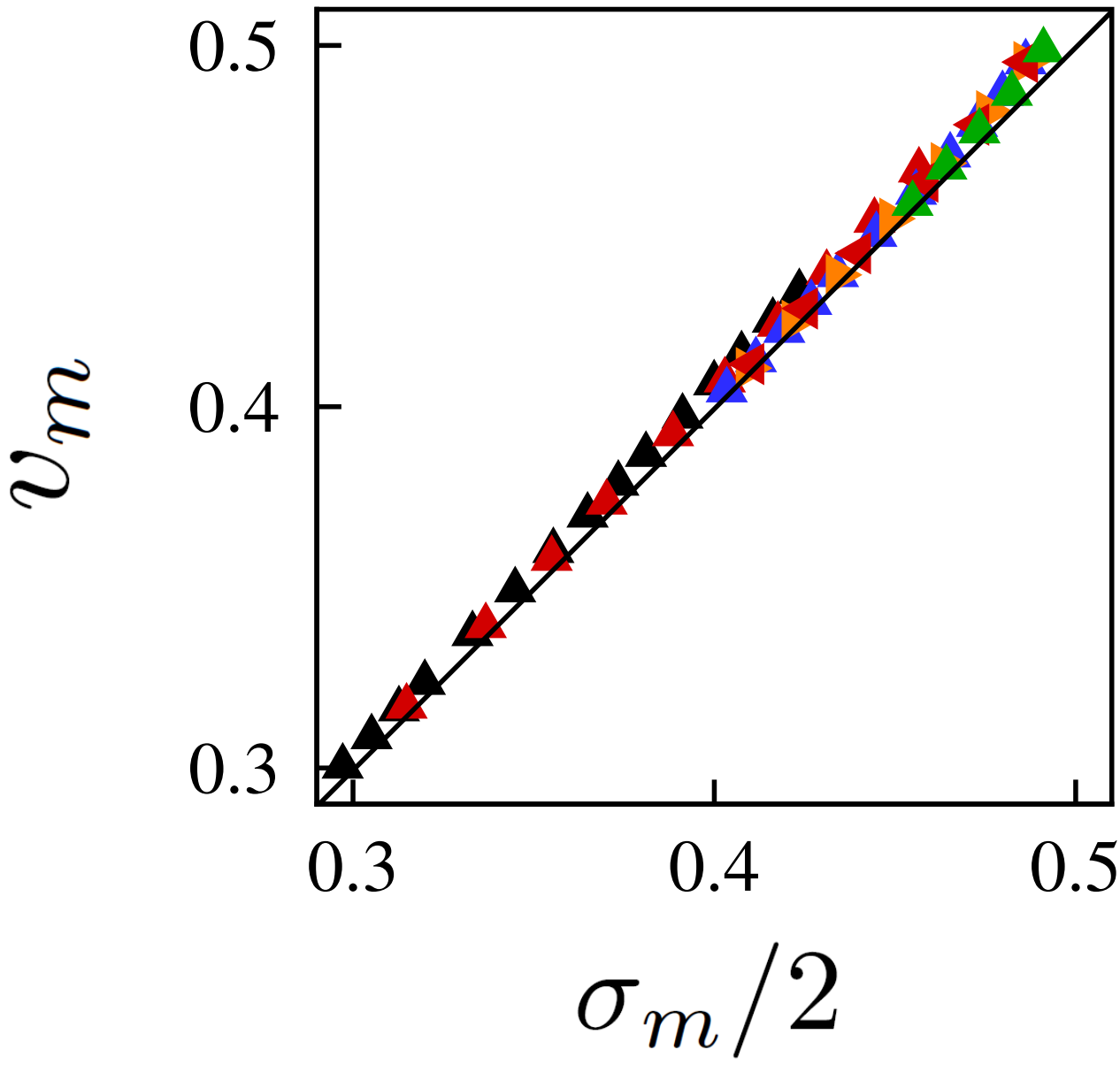

Figure 3: **Effect of the local surface tension on the velocity of contraction.** Pore velocity varies approximately as $v_m = \sigma_m/2$ (solid line). The symbols indicate results from simulations with Ma $= 5 \times 10^{-4}$ (green), 1×10^{-3} (blue), 3×10^{-3} (red) and 5×10^{-3} (black), and Peclet numbers Pe $= 10$ (left triangle), 1×10^{2} (right triangle) and 1×10^{3} (up triangle).

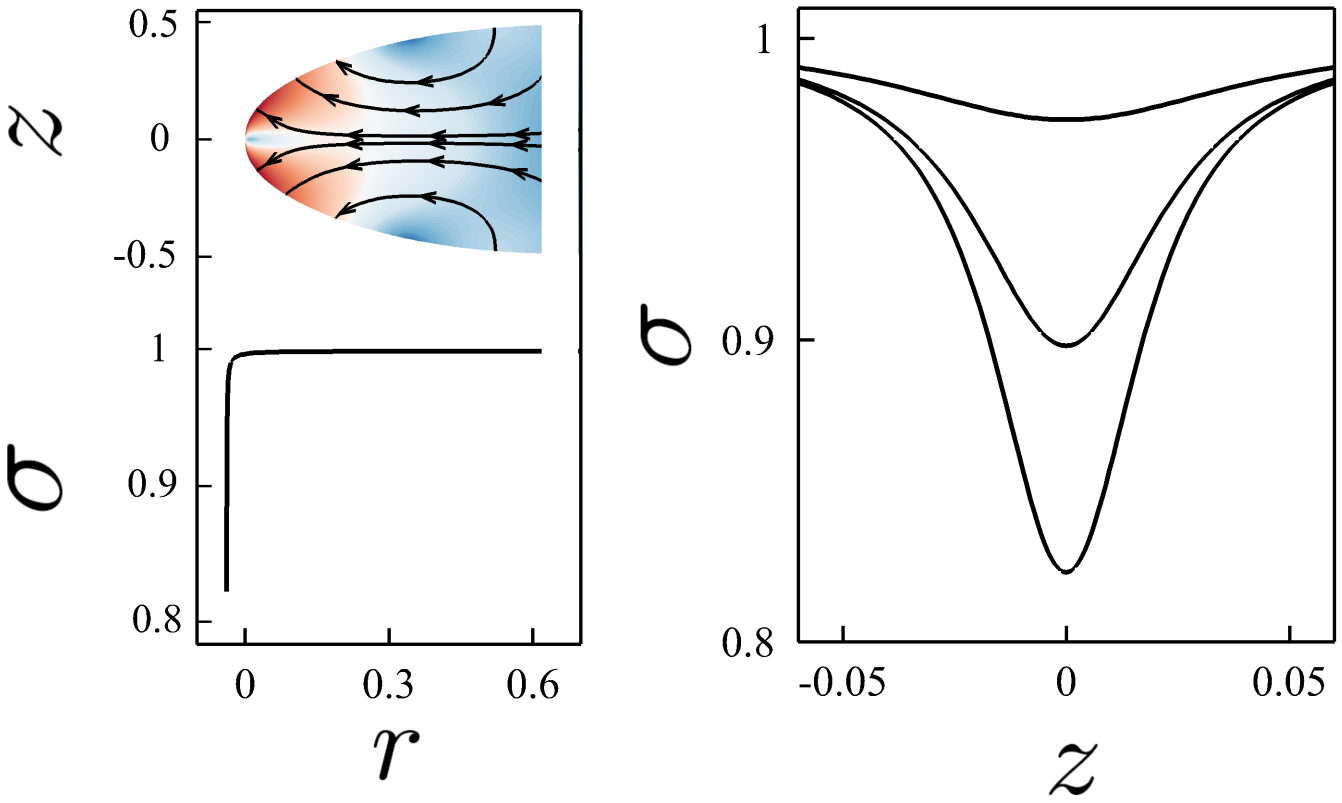

Figure 4: **Spatial evolution of the dynamic surface tension.** Distribution of the instantaneous surface tension σ on the surface of the pore of Figure 2 with $Ma = 1 \times 10^{-3}$. (**a**) Cross sectional fluid velocity and radial distribution of the surface tension for pore radius $r_m = 2.2 \times 10^{-3}$. (**b**) Axial distribution of the surface tension for pore radii $r_m = 2.2 \times 10^{-3}$, 6×10^{-4}, and 3.4×10^{-4} (from top to bottom).

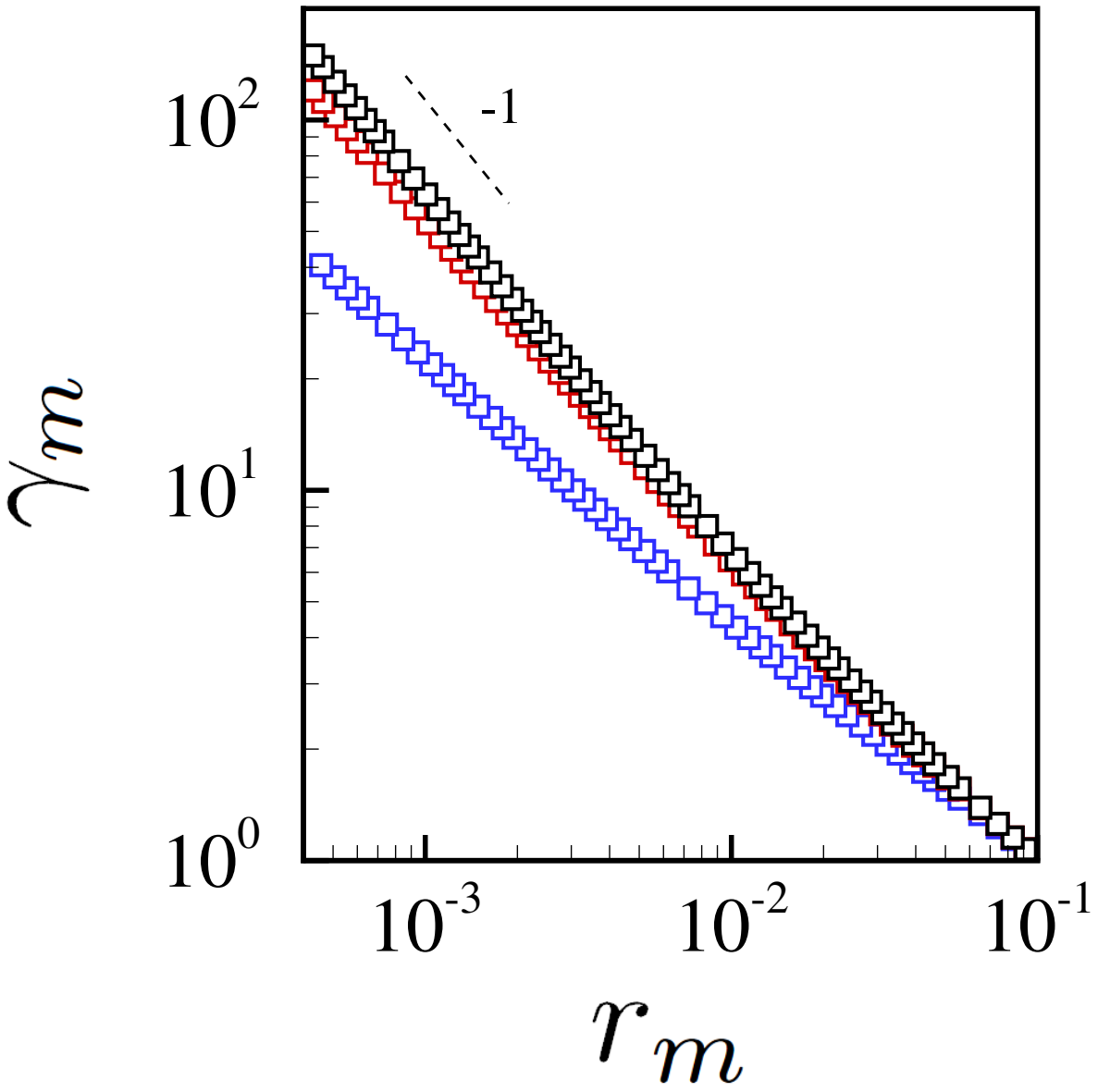

Figure 5: **Scaling of surfactant concentration with pore radius.** Surfactant concentration at the pore tip eventually follows the scaling $\gamma_m \sim r_m^{-1}$ for moderate and large Peclet numbers. Here, $Ma = 0.001$ and $Pe = 10$ (blue), 100 (red), 1×10^3 (black), and 1×10^4 (black). The results for $Pe = 1 \times 10^3$ and 1×10^4 overlap.

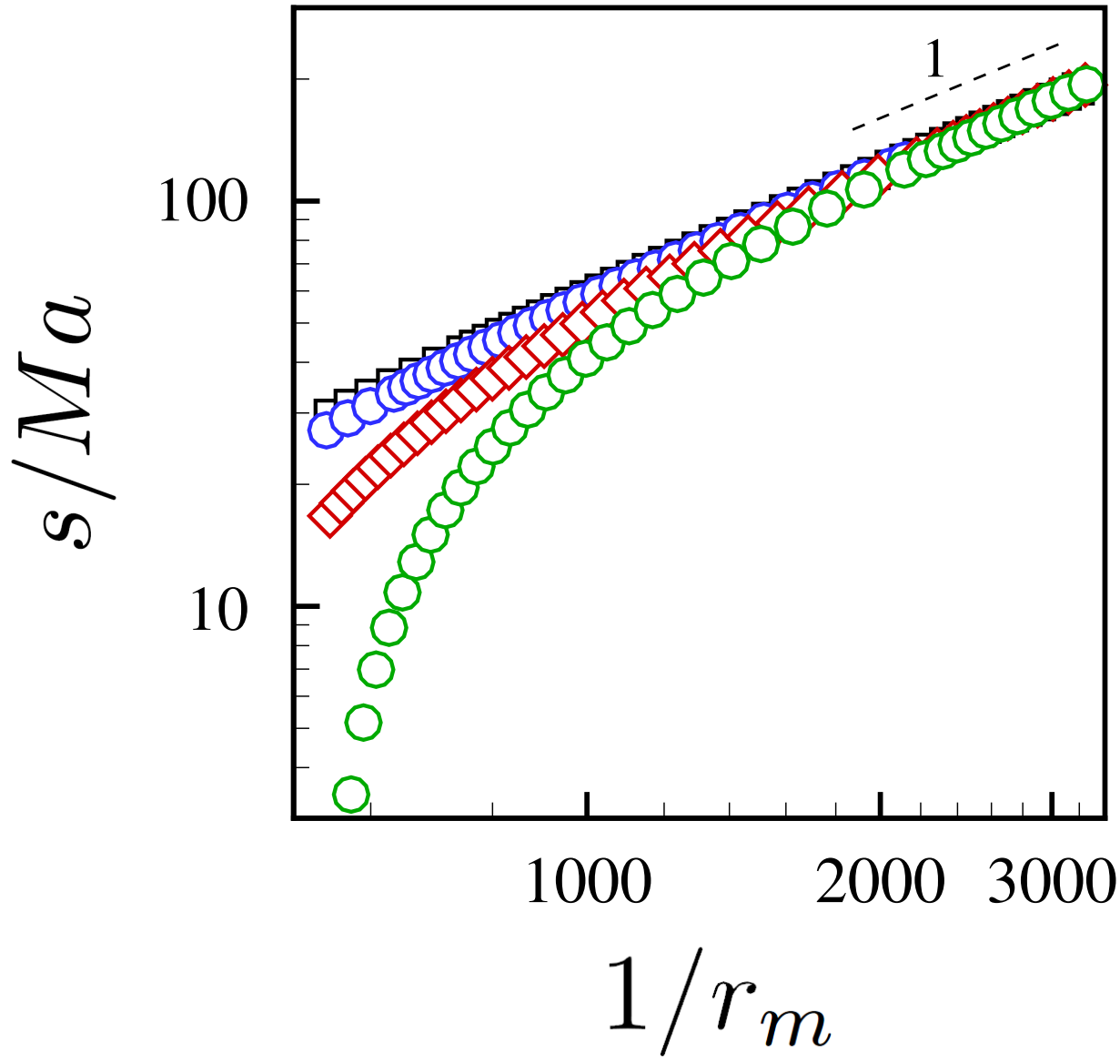

Figure 6: **Scaling of pore velocity with pore radius.** Scaling of normalized velocity s with inverse pore radius for pores with Ma = 0.0005 (green), 0.001 (red), 0.003 (blue), and 0.005 (black).

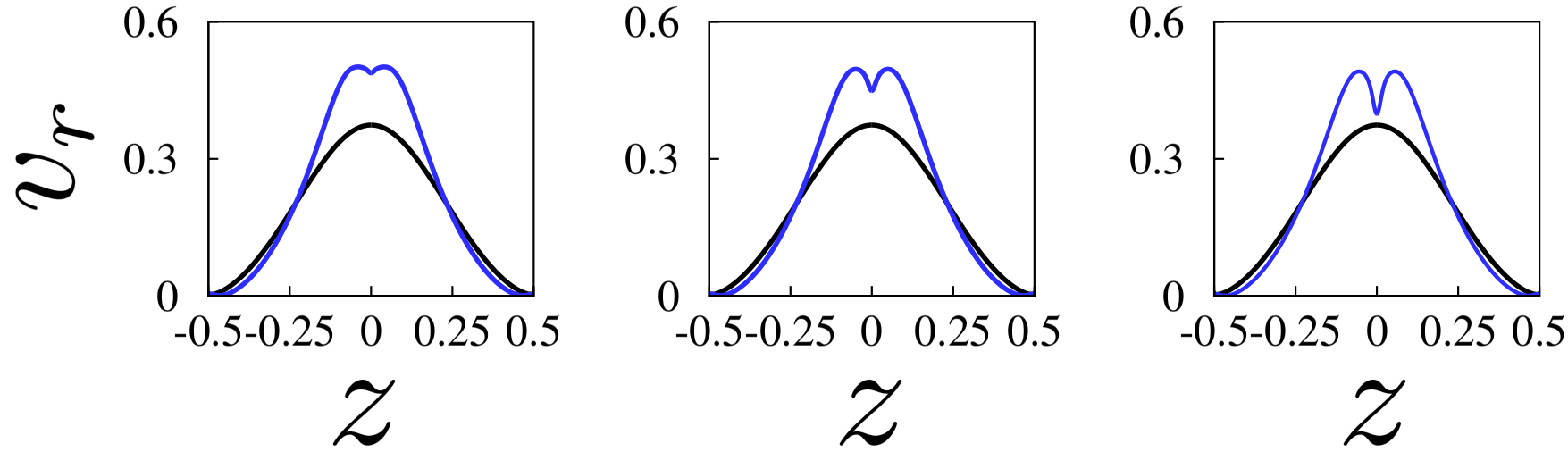

Figure 7: **Influence of Marangoni number on interfacial velocity profiles.** Interfacial radial velocity for contracting pores with $Ma = 0.0001$ (left), 0.0005 (middle), and 0.001 (right). Results correspond to pore radius $r_m = 0.095$ (black) and 0.0003 (blue).

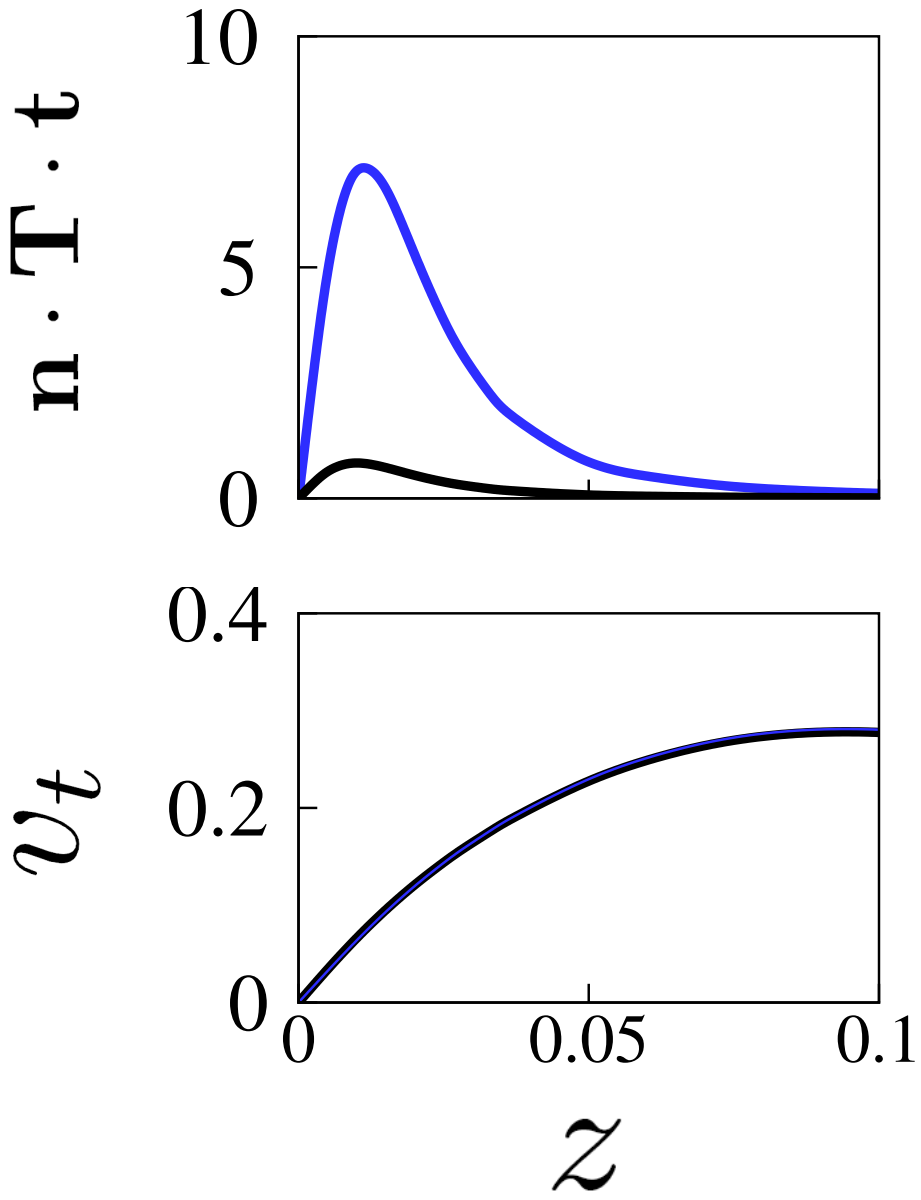

Figure 8: **Marangoni stresses and tangential interfacial flow.** (**a**) Axial variation of tangential Marangoni stress on the surface of the pores of Figure 7 with Ma $= 1 \times 10^{-4}$ (blue) and 1×10^{-3} (black) at pore radius $r_m = 3 \times 10^{-4}$. (**b**) The corresponding tangential interfacial velocities v_t overlap.